Gold Metasurfaces as Saturable Absorbers for All-Normal-Dispersion Ytterbium-Doped Mode-Locked Fiber Laser

Zhijin Chen [ID], Lili Gui [ID], Chuanshuo Wang, Xiaosheng Xiao [ID], *Senior Member, IEEE*, Chao Meng, Sergey I. Bozhevolnyi [ID], Tian Zhang [ID], Xiaoguang Zhang [ID], and Kun Xu [ID]

Abstract—Optical metasurfaces, i.e., thin planar structures with subwavelength metal or dielectric unit cells, have attracted great interest due to their intriguing capabilities of shaping light in both linear and nonlinear regimes. However, their saturable absorption properties and corresponding applications have so far been rarely exploited. Here we report on passively mode-locked ytterbium-doped fiber lasers utilizing saturable metasurfaces made of periodically arranged gold nanorods. Three 400-nm-period metasurfaces with gold nanorods of different lengths (from 210 to 240 nm) and plasmonic resonances (from 968 to 1044 nm) are fabricated and found to exhibit nonlinear absorption with decent modulation depths, facilitating the formation of mode-locking states at 1060 nm. The corresponding lasers generate typically mode-locked pulses with the duration of ∼ 62.3 ps, repetition rate of 10.33 MHz, and signal-to-noise ratio of ∼74 dB. Our experimental results demonstrate that the gold nanorod-based metasurfaces can be used as relatively broadband mode-lockers in the 1-μm-wavelength range.

Index Terms—Metamaterials, mode-locked lasers.

I. INTRODUCTION

MODE-LOCKED fiber lasers are widely used in optical communication [1], material processing [2], as well as medicine and fundamental research [3], [4] due to their robustness and compactness [5], [6]. There are active and passive

Zhijin Chen, Lili Gui, Chuanshuo Wang, Xiaosheng Xiao, Tian Zhang, Xiaoguang Zhang, and Kun Xu are with the State Key Laboratory of Information Photonics and Optical Communications, Beijing University of Posts and Telecommunications, Beijing 100876, China (e-mail: jindaohei@bupt.edu.cn; liligui@bupt.edu.cn; wangcs1997@126.com; xsxiao@bupt.edu.cn; ztian@bupt.edu.cn; xgzhang@bupt.edu.cn; xukun@bupt.edu.cn).

Chao Meng and Sergey I. Bozhevolnyi are with the SDU Nano Optics, University of Southern Denmark, Campusvej 55 DK-5230 Odense, Denmark (e-mail: 04cmeng@gmail.com; seib@mci.sdu.dk).

mode-locking methods according to the associated mechanisms. Active mode-locking techniques mainly employ electro-optic [7], and acousto-optic modulators [8], etc. Generally, actively mode-locked lasers suffer from bulky sizes, high costs, and weak peak power due to the presence of modulators in the cavity [9]. Compared to active counterparts, passively mode-locked lasers require simpler configurations with lower costs. A nonlinear optical component - saturable absorber (SA) [10], plays a key role in achieving passive mode-locking states. Owing to their saturable absorption properties [i.e., absorption decrease with upgrading incident optical power] [11], SAs can transform the continuous-wave (CW) lasing into a train of ultrashort optical pulses under certain conditions. At the same time, semiconductor saturable absorber mirrors (SESAMs) [12] that are currently commercial mode-lockers suffer from narrow operation wavelength ranges and sophisticated manufacturing processes [13]. Many novel materials have been exploited as SAs, including carbon-based materials including carbon nanotubes [6] and graphene [13], topological insulators (TIs) [14], transition metal dichalcogenides (TMDs) [15], black phosphorus (BP) [16], antimonene [17], bismuthene [18], and MXene [19], etc. Metallic nanostructures are promising candidates due to their relatively large third-order nonlinearities [20], wideband absorption (associated with plasmonic resonances), and fast response time [21]. Gold nanorods (GNRs) as SAs for mode-locked lasers or Q-switched lasers have experimentally been demonstrated [22]–[26]. However, the mainstream synthesis methods like seed-mediated growth method [27]–[29], result in solution samples containing dissimilar GNRs with dispersed dimensions (and therefore resonance wavelengths) and random directions, a circumstance that hinders accurate performance control.

Optical metasurfaces, two-dimensional thin planar structures composed of subwavelength metal or dielectric units, have ignited our imagination to realize a new generation of planar optical elements with unique functions for numerous potential applications [30]. Metasurfaces enable the control over reflected and transmitted optical fields by manipulating their amplitudes, phases, polarization states, and so on [31]. Due to their ultrathin geometry, metasurfaces are easy to integrate into other devices [32]. There have been a series of practical applications such as metalenses [33] and hologram [34], among others [31]. Metasurfaces can additionally be utilized to tailor nonlinear optical
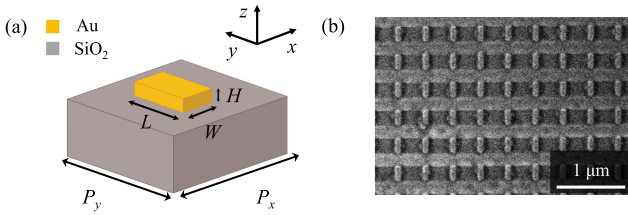
Fig. 1. (a) The unit cell of the metasurface samples, and (b) the SEM image (top view) of the metasurface with $L = 210$ nm, $W = 60$ nm, $H = 45$ nm, $P_x = P_y = 400$ nm.

Fig. 2. Linear transmission spectra of the metasurface samples with differently sized GNRs arrays for incident linearly y-polarized light: (a) simulation and (b) experimental results. Blue, red, and black curves represent the results for metasurfaces with nanorod long-side length $L_1 = 210$ nm, $L_2 = 230$ nm, and $L_3 = 240$ nm, respectively.

processes [35], e.g., second-harmonic generation [36], boosted up by the associated resonances and electromagnetic local-field enhancement. Saturable absorption properties of semiconductor metasurfaces [37] and intersubband polaritonic metasurfaces [38] have been studied very recently. Furthermore, resonant saturable plasmonic metasurfaces have also been explored for achieving passive mode-locking in fiber lasers and generating ultrashort optical pulses at the wavelength of 1.5 μm [39]. There has however been no report on passively mode-locked lasers at other wavelength regions by using metasurface-based SAs. Besides, the nonlinear absorption properties of resonant metasurfaces in terms of operation bandwidth, robustness (with respect to geometrical parameters realized), and polarization sensitivity need further investigations.

In present work, we report on passively mode-locked ytterbium-doped fiber laser (YDFL) operating in the 1-μm-wavelength range that utilize, as SAs, resonant plasmonic metasurfaces comprising periodic GNRs. The near-field enhancement generated by GNRs of different lengths (and featuring therefore different resonance wavelengths) is numerically analyzed as a function of the wavelength, promising relatively broad operation bandwidths when being used as saturable metasurfaces. Three 400-nm-period metasurfaces with gold nanorods of different lengths (varying over 30 nm) and plasmonic resonances (from 968 to 1044 nm) are fabricated and found to exhibit nonlinear absorption with decent modulation depths, facilitating the formation of mode-locking states at 1060 nm. An assembled fiber laser operates typically at 1060.6 nm with a 1.86-nm spectral bandwidth and emits ~62.3 ps pulses with a repetition rate of 10.33 MHz. A high signal-to-noise ratio (SNR) of ~74 dB at fundamental rate has been obtained for the RF spectrum of the pulse train, indicating stable pulse operation. To the best of our knowledge, this is the first demonstration of non-linear metasurfaces for all-normal-dispersion ytterbium-doped mode-locked fiber laser. Meanwhile, our work systematically analyzes the relationship between SA properties and near-field enhancement, further confirming the wide SA properties and mode-locking ability of gold-nanorod metasurfaces.

II. CHARACTERIZATION OF GOLD METASURFACES SA

The metasurfaces consist of periodic GNR arrays with size of 100 μm$\times$ 100 μm, prepared by standard electron-beam lithography and lift-off process. A unit cell of the metasurface samples is schematically shown in Fig. 1(a), where the bottom
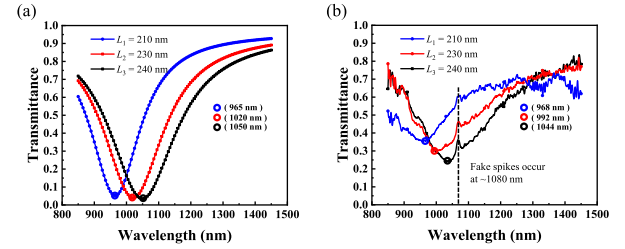
layer is SiO$_2$ substrate, and the top layer is a GNR. The nominal geometric parameters of the GNR are as follows: length L ranging from 210 nm to 240 nm, width $W = 60$ nm, and thickness $H = 45$ nm. The periods of the metasurfaces along x- and y-direction are $P_x = P_y = 400$ nm respectively. Fig. 1(b) depicts the scanning-electron-microscope (SEM) image of the periodic GNRs with length of 210 nm.

The saturable absorption is activated by the local-field enhancement associated with localized surface plasmon resonance (LSPR) of the metasurfaces. Owing to LSPR, strong light-matter interaction occurs at resonances, resulting in large absorption and reflection of light and small transmission at the corresponding resonance wavelength. By carefully designing relevant geometric parameters of the unit cell as described above, it is possible to tune the LSPR position of the plasmonic metasurface to the wavelength region of ~1 μm, which would be used for enabling a mode-locked laser at this wavelength regime. The linear transmission spectra of the three plasmonic metasurfaces with lengths $L_1 = 210$ nm, $L_2 = 230$ nm, $L_3 = 240$ nm are shown in Fig. 2 with both simulation and experiment. The simulation was performed using finite element method while the experimental results were measured by a home-made setup using a broadband supercontinuum as the light source. In both simulation and experiment, light beam polarized along y-direction [Fig. 1(a)] is normally incident onto the samples, and longitudinal LSPR modes are excited. It can be visualized that the valleys of the transmission spectra locate around 1 μm region for all three metasurface samples. The dip values of transmission spectra of the three arrays (blue, red, and black curves in Fig. 2 respectively) in simulation [Fig. 2(a)] are 965 nm, 1020 nm, and 1050 nm, and corresponding experimental results [Fig. 2(b)] are 968 nm, 992 nm, and 1044 nm, respectively. These results confirm that larger aspect ratio of the plasmonic nanorods can lead to LSPR at longer wavelength. Differences occur between simulation and measurement mostly owing to fabrication imperfections and mismatch of the dielectric constant of materials. Noteworthily, since the supercontinuum has a sharp peak at ~1080 nm and its power is not very stable, small but fake spikes around the same region appear for all three samples in Fig. 2(b). We also need to mention that the resonance widths of about 100 nm or 200 nm for all three samples are very typical for plasmonic nanostructures that include considerable damping losses. In order to understand the saturable absorption
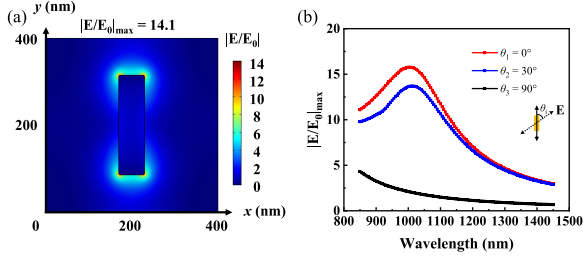
Fig. 3. Simulation results for the metasurface with $L_2 = 230$ nm. (a) Electric near-field distributions at light wavelength of 1060 nm at the plane of the half height of the gold nanorod. The incident linear polarization is along the long axis of the nanorods. (b) The relationship between the electric-field enhancement and wavelength at different polarization angles.

TABLE I
CALCULATED FIELD ENHANCEMENT OF THE METASURFACES WITH
DIFFERENTLY SIZED NANOROD ARRAYS AT RESONANT, MODE-LOCKING
OPERATION, AND FAR OFF-RESONANT WAVELENGTHS

Array	Wavelength (nm)	$|\mathbf{E}/\mathbf{E}_0|_{max}$
$L_1 = 210$ nm	965	20.8
	1035	15.1
	1060	12.9
	1450	2.6
$L_2 = 230$ nm	1020	15.6
	1035	15.2
	1060	14.1
	1450	2.9
$L_3 = 240$ nm	1035	13.5
	1050	13.6
	1060	13.5
	1450	3.1

properties versus the local-field enhancement, we performed careful numerical calculations of the electrical field distribution in the vicinity of a nanorod, whose corners were rounded with the radius of 5 nm to avoid field singularities [40]. Fig. 3(a) depicts electric-field distributions at the nanoscale at 1060 nm of the array with $L_2 = 230$ nm. Due to the LSPR, the electrical field is strongly enhanced with the maximum near-field enhancement $|\mathbf{E}/\mathbf{E}_0|_{max}$ reaching ~14.1. The one-order-of-magnitude larger local electric field compared with incident counterpart is very typical for plasmonic systems [41], which is also the origin for enhanced second- and third-order nonlinear frequency conversion processes in previous works [35]. Note that the calculated field enhancement is influenced by the corner rounding used and thus might deviate from what actually takes place in the experiment, but qualitative relationships should still hold, providing us with the fundamental insight on saturable absorption of resonant metasurfaces. Fig. 3(b) shows the relationship between the electric-field enhancement and wavelength at different polarization angles. Apparently, when the polarization angle θ is 0° (namely, incident light polarized along y-direction), the array exhibits largest field enhancement at almost the resonant wavelength, and the spectrum gives a linewidth around 400 nm. The field enhancement covering a large wavelength range indicates a broadband saturable absorption that might occur in experiment. With increasing the polarization angle θ, the field enhancement becomes weaker, owing to the less efficient excitation of the longitudinal LSPR mode. It is worth mentioning that when the polarization angle is 90°, only transverse LSPR mode is excited, with corresponding resonant wavelength at about 680 nm, and thus the field enhancement around 1 μm is very small, as expected.

Quantitatively, the corresponding field enhancement $|\mathbf{E}/\mathbf{E}_0|_{max}$ of different arrays on resonance and off resonance is listed in detail respectively in Table I. It can be seen that the local field is always greatest at the resonant wavelength, but considerable field enhancement can still be achieved at 1035 nm or 1060 nm (the spectral region where saturable absorption properties were measured or used for mode-locking in experiment) compared with the far off-resonant position (1450 nm) for all three metasurface samples. It may lead to broadband nonlinear absorption performances of the
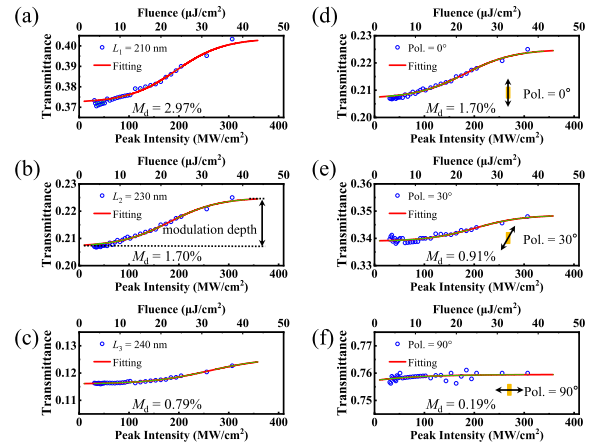

Fig. 4. Nonlinear transmission measurement of three metasurface samples with differently sized gold nanorods. Results for the arrays with length $L_1 = 210$ nm, $L_2 = 230$ nm, and $L_3 = 240$ nm are given in (a)–(c), respectively. Incident polarization is along y-axis. Results for the array with $L_2 = 230$ nm at different polarization directions of the incident light are given in (d)–(f). The angles between polarization direction and y-direction are 0°, 30° and 90°, respectively.

metasurfaces, and relax the demand of rigorous geometrical control of the nanostructures during fabrication.

Nonlinear transmission measurement for gold plasmonic metasurfaces was performed by launching a mode-locked laser (center wavelength of 1035 nm, pulse width of 122 fs, and repetition rate of 50.1 MHz) onto the samples. As depicted in Fig. 4(a)–(c), all three gold plasmonic metasurfaces (i.e., with different long-side length L) exhibit saturable absorption behaviors, where the blue circles denote the experimental results and the red curves are S-shape fitting. Limited by the measurement range of our power meters, we did not achieve complete saturation of the absorption. Hence, we use S-profile to fit the measurement results, as in [39]. Modulation depth is a critical parameter to evaluate the performance of a saturable absorber, which can be defined as the difference between maximum and minimum transmittance in the nonlinear transmission measurement. The modulation depths M_d of the metasurfaces with $L_1 = 210$ nm, $L_2 = 230$ nm, and $L_3 = 240$ nm are 2.97%, 1.70%, and 0.79%, respectively. The magnitude of the modulation depth as
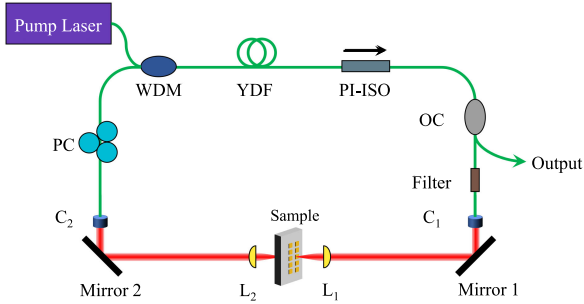
Fig. 5. Schematic diagram of the ytterbium-doped mode-locked fiber laser based on gold metasurfaces as SAs.
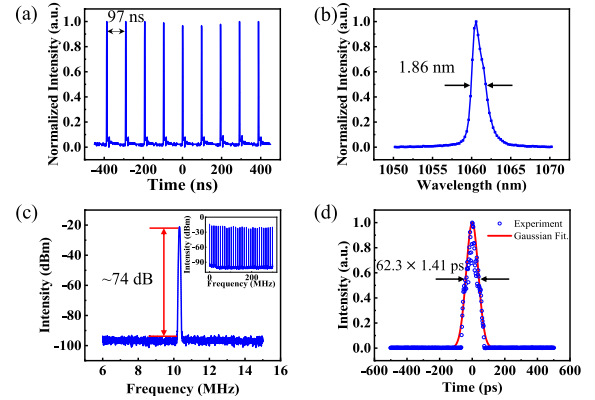

Fig. 6. The typical laser output properties: (a) the typical pulse train, (b) the optical spectrum, (c) the corresponding RF spectrum at 10.33 MHz (Inset: RF spectrum measured over a 0-300 MHz span), and (d) the corresponding autocorrelation trace. The metasurface with $L_2 = 230$ nm was employed.

well as the fluence where saturable absorption can be observed locates at the similar level as other nonlinear nanomaterials such as Bi_2Se_3 [42]. For a higher modulation depth, one can design a novel plasmonic metasurface with stronger field enhancement, or introduce other nonlinear materials (like graphene [43]) into the pure gold nanostructures, to fabricate hybrid metasurfaces. Furthermore, we measured the nonlinear transmittance of the metasurface with $L_2 = 230$ nm for incident light with different linear polarization orientations, as shown in Fig. 4(d)–(f). Obviously, modulation depths decrease with increasing the polarization angle, as expected by the field-enhancement simulation shown in Fig. 3(b). The LSPR near 1 μm is most efficiently excited by incident light polarized along y-direction. Based on the above results and analysis, it is well confirmed that the polarization-dependent nonlinear absorption properties of the metasurfaces are directly linked to their local-field enhancement, and we could further tailor the saturation conditions either by flexible structural design (i.e., shape, material, arrangement) or by altering the properties of the excitation light (i.e., polarization state) in the future.

III. EXPERIMENTAL SETUP AND RESULTS

Fig. 5 illustrates the experimental configuration of the ytterbium-doped mode-locked fiber laser based on gold plasmonic metasurface SA. A laser diode (LD) with emission wavelength centered at 976 nm is used as the pump source and delivered into the laser cavity via a 980/1060 nm wavelength division multiplexer (WDM). A segment of 70-cm-long ytterbium-doped fiber (YDF) with a group velocity dispersion (GVD) of approximately $\sim$23.26 ps^2/km at 1060 nm serves as a gain medium. A polarization-insensitive isolator (PI-ISO), placed behind the YDF, is utilized to ensure unidirectional operation of the ring cavity. A 10/90 optical coupler (OC) is introduced to extract 10% power of the generated pulses as output for characterization. A band-pass filter centered at 1064 nm with a bandwidth of 8 nm, is employed for self-consistence in the spectral regime after a round-trip propagation. Two collimators (C_1, C_2) are used to realize efficient coupling between the free-space and fiber optical paths with a coupling efficiency of 56%, which means that the power received at the collimator C_2 is approximately 56% of the power emitted from the collimator C_1. Furthermore, the light is focused on the metasurfaces by lens L_1 resulting in a spot within the metasurface region, and restored

to a parallel beam by lens L_2. The length of the free-space path is about 0.6 m. The use of a polarization controller (PC) is for adjusting intracavity polarization states and thus enabling us to finely tune the mode-locking operation of the laser. The optical fiber path is connected by single-mode fiber (SMF) of 18.1 m long with a GVD of approximately $\sim$21.65 ps^2/km at 1060 nm. Therefore, the overall optical fiber section is about 18.8 m long, and the corresponding dispersion is approximately 0.423 ps^2. The output is monitored by a digital oscilloscope, an optical spectrum analyzer, an autocorrelator and a radio-frequency (RF) spectrum analyzer coupled with a photodetector.

We first tested the mode-locking effects by using the metasurface with $L_2 = 230$ nm. When the pump power exceeds the threshold of 149 mW, stable pulse traces are observed after a careful adjustment of PC. The characteristic laser output is illustrated in Fig. 6, measured at a pump power of 300 mW. In this case, the fluence focused on the metasurface are about 40 μJ/cm^2, on the level where saturable absorption of the metasurface occurs [see Fig. 4(b)]. Fig. 6(a) depicts the typical pulse train in time domain. The temporal interval between two adjacent pulses is about 97 ns, corresponding to a repetition rate of $\sim$10.33 MHz, which coincides with the calculated value by using the optical length of the total cavity as well. The output optical spectrum in Fig. 6(b) centers at 1060.6 nm with a 3-dB bandwidth of 1.86 nm. It manifests the feature of fiber lasers in the all-normal dispersion regime [29]. Fig. 6(c) illustrates the corresponding RF spectrum at the fundamental repetition rate of 10.33 MHz with a large SNR of $\sim$74 dB, which indicates good stability of the lasing operation. The inset photograph of Fig. 6(c) shows the RF spectrum over a span of 300 MHz that gives more details of the stability. Fig. 6(d) displays a 3-dB temporal width of $\sim$87.8 ps of the autocorrelation trace corresponding to a pulse width of 62.3 ps if a Gaussian pulse profile is assumed. The calculated time-bandwidth product (TBP) is 30.91, indicating a highly chirped essence of the mode-locked pulses. The large chirp of the pulses is mainly caused by the normal dispersion of the fiber laser, in addition to weak modulation depth of the SA. Shorter pulse width could be achieved if intracavity dispersion
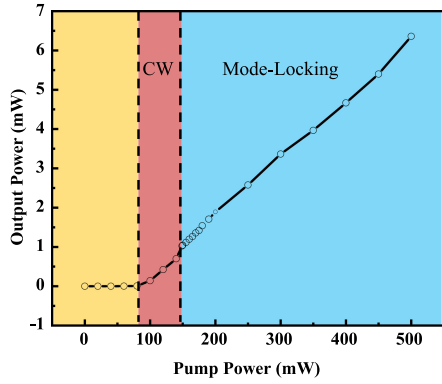
Fig. 7. The output power as a function of the pump power. CW and mode-locked regimes are marked with red and blue shaded areas, respectively. The metasurface with $L_2 = 230$ nm was employed.
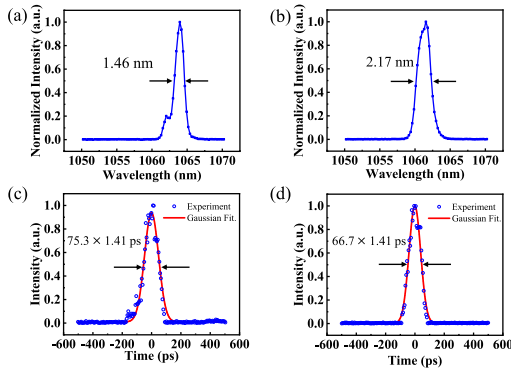

Fig. 8. The typical mode-locking performances of the other two plasmonic metasurfaces. The optical spectra for the arrays with length $L_1 = 210$ nm and $L_3 = 240$ nm are given in (a) and (b), respectively. The corresponding autocorrelation traces for $L_1 = 210$ nm and $L_3 = 240$ nm are given in (c) and (d), respectively.

is carefully controlled, such as achieving net negative dispersion or near-zero dispersion.

Fig. 7 reveals the change of output power as a function of the pump power. CW lasing output are obtained for pump power reaching the range between 80 and 148 mW, while for even larger pump power, the laser operation enters a mode-locking regime. The output power versus pump power in mode-locking regime leads to a slope efficiency of about 1.47%, as shown by the blue shaded area. Larger slope efficiency could be expected if we eject more power from the OC output port, together with better coupling control between free space and optical fiber by elaborate collimation and focusing design.

In addition, the mode-locking performances of the other two plasmonic metasurfaces with long-side length $L_1 = 210$ nm and $L_3 = 240$ nm were also tested with the same laser cavity configuration shown in Fig. 5. Stable mode-locking operation was achieved as well, with Fig. 8 depicting typical spectral and autocorrelation profiles of the mode-locking states. Due to slightly different saturable absorption characteristics, the three plasmonic metasurfaces enable robust mode-locking states with distinguishable spectral and temporal features. The results imply the broadband nature of the saturable absorption of the gold metasurfaces owing to the LSPR resonances. Hence, there is

no rigorous requirement of finely controlling fabrication accuracy of gold metasurfaces. In contrast, the performances of the commercial SAs like SESAMs usually suffer dramatically from lattice mismatch during preparation. Besides, SESAM is also difficult to design as broadband SA.

To unambiguously confirm that the mode-locking states arise from the metasurfaces, we focused the beam directly on the substrate instead of the metasurface area. No matter how we adjusted the PC and/or changed the pump power, only CW operation was achievable. But still, our metasurfaces might introduce nonlinear polarization rotation (NPR) effect in optical path due to their strong polarization-dependent losses, and accordingly, it is difficult to attribute the mode-locking to pure SA properties of the metasurfaces. Instead, we used a polarizer to replace the metasurface in the optical path, to introduce even stronger polarization-dependent loss to the cavity. In this case, no mode-locked pulses were obtained in the experiment. In other words, although we cannot completely exclude the influence of NPR effects, the realization of mode-locking must have made use of the SA properties of the metasurfaces. Most likely, the mode-locking stems from a hybrid mechanism based on the SA properties of the metasurfaces and the residual NPR effects.

IV. CONCLUSION

In summary, we have numerically and experimentally investigated linear and nonlinear optical properties of gold nanorod metasurfaces particularly their saturable absorption. Due to anisotropy, the gold nanorod arrays exhibit adjustable modulation depths which are sensitive to the incident polarization direction. By inserting the plasmonic metasurfaces as a SA in a fiber laser cavity, we experimentally demonstrate a mode-locked fiber laser at 1-μm regime. Mode locked states at $\sim$1 μm were realized by using three metasurfaces with different LSPR wavelengths, owing to the broadband LSPR induced saturable absorption behavior. Typically, the metasurface-based fiber laser could achieve a stable pulsed lasing output with a 1060.6 nm central wavelength, $\sim$62.3 ps pulse width, $\sim$10.33 MHz repetition rate, along with a up to $\sim$74 dB SNR of the RF spectrum. Our experimental demonstration verifies the feasibility and robustness of using gold metasurfaces as SAs for mode-locked fiber lasers at 1 μm region.

In the future, novel metasurfaces involving versatile material compositions and resonance properties can be designed so that saturable absorption properties and functionalities far beyond conventional SAs could be envisioned. For example, metasurfaces could provide manipulation over phase [44], amplitude [45], polarization state [46], and even angular momentum [47] of light at the nanoscale. When in combination with highly nonlinear materials such as epsilon-near-zero materials and graphene [43], [48] etc, nonlinear metasurfaces could add unprecedented degrees of freedom to the ultrafast optics and photonics paradise. Our current work serves as an initial basis and nonlinear metasurfaces might move toward more complex spatial-temporal tailoring of light for more practical usage in the areas of nonlinear optics, integrated optics, and neuromorphic photonics.

REFERENCES

[1] S. Gross and M. J. Withford, "Ultrafast-laser-inscribed 3D integrated photonics: Challenges and emerging applications," *Nanophotonics*, vol. 4, no. 3, pp. 332–352, 2015.

[2] K. Sugioka and Y. Cheng, "Ultrafast lasers—Reliable tools for advanced materials processing," *Light Sci. Appl.*, vol. 3, no. 4, 2014, Art. no. e149.

[3] S. H. Chung and E. Mazur, "Surgical applications of femtosecond lasers," *J. Biophotonics*, vol. 2, no. 10, pp. 557–572, Oct. 2009.

[4] E. Mottay, X. Liu, H. Zhang, E. Mazur, R. Sanatinia, and W. Pfleging, "Industrial applications of ultrafast laser processing," *MRS Bull*, vol. 41, no. 12, pp. 984–992, 2016.

[5] Y. Wang et al., "An all-optical, actively Q-Switched fiber laser by an antimonene-based optical modulator," *Laser Photon. Rev.*, vol. 13, no. 4, 2019, Art. no. 1800313.

[6] L. Hou et al., "Sub-200 femtosecond dispersion-managed soliton ytterbium-doped fiber laser based on carbon nanotubes saturable absorber," *Opt. Exp.*, vol. 26, no. 7, pp. 9063–9070, Apr. 2018.

[7] J. Bogusławski et al., "Graphene actively mode-locked lasers," *Adv. Funct. Mater.*, vol. 28, no. 28, 2018, Art. no. 1801539.

[8] M. Bello-Jiménez, E. Hernández-Escobar, A. Camarillo-Avilés, O. Pottiez, A. Díez, and M. V. Andrés, "Actively mode-locked all-fiber laser by 5 MHz transmittance modulation of an acousto-optic tunable bandpass filter," *Laser Phys. Lett.*, vol. 15, no. 8, 2018, Art. no. 085113.

[9] L. Xiao-Hui et al., "Wavelength-switchable and wavelength-tunable all-normal-dispersion mode-locked yb-doped fiber laser based on single-walled carbon nanotube wall paper absorber," *IEEE Photon. J.*, vol. 4, no. 1, pp. 234–241, Feb. 2012.

[10] C. Ma, C. Wang, B. Gao, J. Adams, G. Wu, and H. Zhang, "Recent progress in ultrafast lasers based on 2D materials as a saturable absorber," *Appl. Phys. Rev.*, vol. 6, no. 4, 2019, Art. no. 041304.

[11] B. Zhang et al., "Recent progress in 2D material-based saturable absorbers for all solid-state pulsed bulk lasers," *Laser Photon. Rev.*, vol. 14, no. 2, 2019, Art. no. 1900240.

[12] V. E. Kisel et al., "High-power, efficient, semiconductor saturable absorber mode-locked Yb:KGW bulk laser," *Opt. Lett.*, vol. 40, no. 12, pp. 2707–2710, Jun. 2015.

[13] M. Pawliszewska, T. Martynkien, A. Przewloka, and J. Sotor, "Dispersion-managed Ho-doped fiber laser mode-locked with a graphene saturable absorber," *Opt. Lett.*, vol. 43, no. 1, pp. 38–41, Jan. 2018.

[14] P. Yan, R. Lin, S. Ruan, A. Liu, and H. Chen, "A 2.95 GHz, femtosecond passive harmonic mode-locked fiber laser based on evanescent field interaction with topological insulator film," *Opt. Exp.*, vol. 23, no. 1, pp. 154–164, Jan. 2015.

[15] B. Chen, X. Zhang, K. Wu, H. Wang, J. Wang, and J. Chen, "Q-switched fiber laser based on transition metal dichalcogenides MoS_2, $MoSe_2$, Ws_2, and WSe_2," *Opt. Exp.*, vol. 23, no. 20, pp. 26723–26737, Oct. 2015.

[16] J. Sotor, G. Sobon, W. Macherzynski, P. Paletko, and K. M. Abramski, "Black phosphorus saturable absorber for ultrashort pulse generation," *Appl. Phys. Lett.*, vol. 107, no. 5, 2015, Art. no. 051108.

[17] M. Wang, F. Zhang, Z. Wang, Z. Wu, and X. Xu," *Opt. Exp.*, vol. 26, no. 4, pp. 4085–4095, Feb. 2018.

[18] B. Guo et al., "Sub-200 fs soliton mode-locked fiber laser based on bismuthene saturable absorber," *Opt. Exp.*, vol. 26, no. 18, pp. 22750–22760, Sep. 2018.

[19] Y. I. Jhon et al., "Metallic MXene saturable absorber for femtosecond mode-locked lasers," *Adv. Mater.*, vol. 29, no. 40, Oct. 2017, Art. no. 1702496.

[20] H. B. Liao, R. F. Xiao, J. S. Fu, P. Yu, G. K. L. Wong, and P. Sheng, "Large third-order optical nonlinearity in $Au:SiO_2$ composite films near the percolation threshold," *Appl. Phys. Lett.*, vol. 70, no. 1, pp. 1–3, 1997.

[21] H. B. Liao, R. F. Xiao, H. Wang, K. S. Wong, and G. K. L. Wong, "Large third-order optical nonlinearity in $Au:TiO_2$ composite films measured on a femtosecond time scale," *Appl. Phys. Lett.*, vol. 72, no. 15, pp. 1817–1819, 1998.

[22] Z. Kang et al., "Mode-locked thulium-doped fiber laser at 1982 nm by using a gold nanorods saturable absorber," *Laser Phys. Lett.*, vol. 12, no. 4, 2015, Art. no. 045105.

[23] J. Lee, J. Koo, and J. H. Lee, "Femtosecond mode-locking of an ytterbium-doped fiber laser using self-assembled gold nanorods," *Laser Phys. Lett.*, vol. 14, no. 9, 2017, Art. no. 090001.

[24] X.-D. Wang, Z.-C. Luo, H. Liu, M. Liu, A.-P. Luo, and W.-C. Xu, "Microfiber-based gold nanorods as saturable absorber for femtosecond pulse generation in a fiber laser," *Appl. Phys. Lett.*, vol. 105, no. 16, 2014, Art. no. 161107.

[25] X. Wang et al., "Versatile mode-locked patterns in a fiber laser using silica-coated gold nanorods as saturable absorber," *Laser Phys.*, vol. 30, no. 6, 2020, Art. no. 065104.

[26] Y. W. Lee, C. M. Chen, W. H. Chuang, C. Y. Cho, C. H. Yu, and M. C. Paul, "Highly efficient mode-locked and Q-switched Er^{3+}-doped fiber lasers using a gold nanorod saturable absorber," *Sci. Rep.*, vol. 11, no. 1, Oct. 2021, Art. no. 20079.

[27] Y. Shu et al., "Gold nanorods as saturable absorber for harmonic soliton molecules generation," *Front. Chem.*, vol. 7, 2019, Art. no. 715.

[28] X. Wang et al., "A microfiber-based gold nanorod saturable absorber with evanescent field interaction for multi-soliton patterns in a fiber laser," *Laser Phys.*, vol. 26, no. 6, 2016, Art. no. 065105.

[29] Z. Kang, X. J. Gao, L. Zhang, Y. Feng, G. S. Qin, and W. P. Qin, "Passively mode-locked fiber lasers at 1039 and 1560 nm based on a common gold nanorod saturable absorber," (in English), *Opt. Mater. Exp.*, vol. 5, no. 4, pp. 794–801, Apr. 2015.

[30] A. E. Minovich, A. E. Miroshnichenko, A. Y. Bykov, T. V. Murzina, D. N. Neshev, and Y. S. Kivshar, "Functional and nonlinear optical metasurfaces," *Laser Photon. Rev.*, vol. 9, no. 2, pp. 195–213, 2015.

[31] F. Ding, A. Pors, and S. I. Bozhevolnyi, "Gradient metasurfaces: A review of fundamentals and applications," *Rep. Prog. Phys.*, vol. 81, no. 2, Feb. 2018, Art. no. 026401.

[32] S. S. Bukhari, J. Vardaxoglou, and W. Whittow, "A metasurfaces review: Definitions and applications," *Appl. Sci.*, vol. 9, no. 13, 2019, Art. no. 2727.

[33] S. Wang et al., "Broadband achromatic optical metasurface devices," *Nature Commun.*, vol. 8, no. 1, Aug. 2017, Art. no. 187.

[34] G. Zheng, H. Muhlenbernd, M. Kenney, G. Li, T. Zentgraf, and S. Zhang, "Metasurface holograms reaching 80% efficiency," *Nature Nanotechnol.*, vol. 10, no. 4, pp. 308–312, Apr. 2015.

[35] G. Li, S. Zhang, and T. Zentgraf, "Nonlinear photonic metasurfaces," *Nature Rev. Mater.*, vol. 2, no. 5, 2017, Art. no. 17010.

[36] S. Chen, B. Reineke, G. Li, T. Zentgraf, and S. Zhang, "Strong nonlinear optical activity induced by lattice surface modes on plasmonic metasurface," *Nano Lett.*, vol. 19, no. 9, pp. 6278–6283, Sep. 2019.

[37] V. V. Zubyuk et al., "Low-power absorption saturation in semiconductor metasurfaces," *ACS Photon.*, vol. 6, no. 11, pp. 2797–2806, 2019.

[38] S. A. Mann et al., "Ultrafast optical switching and power limiting in intersubband polaritonic metasurfaces," *Optica*, vol. 8, no. 5, pp. 606–613, 2021.

[39] J. Wang et al., "Saturable plasmonic metasurfaces for laser mode locking," *Light Sci. Appl.*, vol. 9, no. 1, 2020, Art. no. 50.

[40] T. Søndergaard and S. Bozhevolnyi, "Slow-plasmon resonant nanostructures: Scattering and field enhancements," *Phys. Rev. B*, vol. 75, no. 7, 2007, Art. no. 073402.

[41] B. Metzger et al., "Doubling the efficiency of third harmonic generation by positioning ITO nanocrystals into the hot-spot of plasmonic gap-antennas," *Nano Lett.*, vol. 14, no. 5, pp. 2867–2872, May 2014.

[42] Z. Dou, Y. Song, J. Tian, J. Liu, Z. Yu, and X. Fang, "Mode-locked ytterbium-doped fiber laser based on topological insulator: Bi_2Se_3," *Opt. Exp.*, vol. 22, no. 20, pp. 24055–24061, Oct. 2014.

[43] M. Z. E. Rafique, A. Basiri, J. Bai, J. Zuo, and Y. Yao, "Graphene-Plasmonic hybrid metasurface saturable absorber," in *Proc. OSA Adv. Photon. Congr.*, Washington, DC, USA, 2021, Paper M5B.3.

[44] A. C. Overvig et al., "Dielectric metasurfaces for complete and independent control of the optical amplitude and phase," *Light Sci. Appl.*, vol. 8, 2019, Art. no. 92.

[45] G. Y. Lee et al., "Complete amplitude and phase control of light using broadband holographic metasurfaces," *Nanoscale*, vol. 10, no. 9, pp. 4237–4245, Mar. 2018.

[46] H. L. Zhu, S. W. Cheung, K. L. Chung, and T. I. Yuk, "Linear-to-Circular polarization conversion using metasurface," *IEEE Trans. Antennas Propag.*, vol. 61, no. 9, pp. 4615–4623, Sep. 2013.

[47] E. Karimi, S. A. Schulz, I. De Leon, H. Qassim, J. Upham, and R. W. Boyd, "Generating optical orbital angular momentum at visible wavelengths using a plasmonic metasurface," *Light Sci. Appl.*, vol. 3, no. 5, 2014, Art. no. e167.

[48] M. Z. Alam, S. A. Schulz, J. Upham, I. De Leon, and R. W. Boyd, "Large optical nonlinearity of nanoantennas coupled to an epsilon-near-zero material," *Nature Photon.*, vol. 12, no. 2, pp. 79–83, 2018.